Contents lists available at ScienceDirect

Nuclear Instruments and Methods in Physics Research A

Monte Carlo-based evaluation of inter-crystal scatter and penetration in the PET subsystem of three GE Discovery PET/CT scanners

N. Zeraatkar [a], M.R. Ay [a,b,c,*], P. Ghafarian [d], S. Sarkar [a,b], P. Geramifar [a,c], A. Rahmim [e,f]

[a] Research Center for Science and Technology in Medicine, Tehran University of Medical Sciences, Tehran, Iran
[b] Department of Medical Physics and Biomedical Engineering, Tehran University of Medical Sciences, Tehran, Iran
[c] Research Institute for Nuclear Medicine, Tehran University of Medical Sciences, Tehran, Iran
[d] NRITLD, Masih Daneshvari Hospital, Shahid Beheshti University of Medical Sciences, Tehran, Iran
[e] Department of Radiology, Johns Hopkins University, Baltimore, MD, USA
[f] Department of Electrical and Computer Engineering, Johns Hopkins University, Baltimore, MD, USA

ARTICLE INFO

ABSTRACT

While there is continuing demand for higher resolution in PET systems the technological improvements are still challenged by the presence of inter-crystal scatter (ICS) and inter-crystal penetration phenomena in PET detectors, which play an important role in deterioration of the spatial resolution. Both ICS and penetration have deteriorative impact on spatial resolution of PET scanners because they can lead to inaccurate incident crystal assignments. As such, an understanding of the quantitative behavior of ICS and penetration can be beneficial whether for design of a more optimized PET detection system or for more accurate modeling of ICS and penetration effects within the image reconstruction system matrix in order to enhance the quality of reconstructed images. In this work we analyzed the quantity of ICS and penetrated events in the form of coincidences, in contrast with the other studies that have assessed ICS and penetration in the form of single photons. This was performed in the PET subsystem of three GE whole-body PET/CT scanners: Discovery RX (DRX), Discovery ST (DST), and Discovery STE (DSTE). Furthermore, as a novel study, we discriminated between ICS vs. penetration events. In order to do this, we employed the GATE (Geant4 Application for Tomographic Emission) Monte Carlo (MC) toolkit for our simulations and used our previously validated GATE models of the scanners. Developing an algorithm, purely true coincidences were discriminated from ICS- and/or penetration-induced (ICS–P) coincidences. ICS–P coincidences were also categorized into three groups: group-1 consisted of coincidence event(s) only affected by penetration (one or both). Group-2 includes coincidences where one event is affected by ICS (possibly including penetration), while the other event is not affected by ICS (i.e. penetration or no mispositioning at all). Finally in group-3, both events are affected by ICS (possibly also including penetration). The results showed that the most magnificent quantitative variations of ICS-P occur along radial direction. In DRX, more than 55% of the true coincidences are mispositioned due to ICS and/or penetration when the source is located at the end of the transaxial field of view (FOV). This value for DST and DSTE is about 45%. Incidentally, the results revealed that the quantities of ICS–P coincidences in the DST and DSTE are almost equal, while there is much smaller ICS–P in the DRX.

1. Introduction

While there is continuing demand for higher resolution in PET systems, technological improvements are still challenged by the presence of inter-crystal scatter (ICS) and inter-crystal penetration phenomena in detectors [1]. Penetration (exhibiting itself in the form of the so-called parallax effect) occurs when a photon passes through a crystal on which it is incident with no interaction and is instead detected in another crystal. The penetration effect is therefore probable only for photons entering the crystal at non-perpendicular angles and intensifies as the photon energy increases and/or the attenuation coefficient of the detector material decreases. Hence, the probability of a 511 keV photon in a PET system for penetrating through the incident crystal with no interaction is considerable. On the other hand, ICS can be present even for photons incident perpendicularly to the crystal and happens when a photon escapes from the crystal it initially
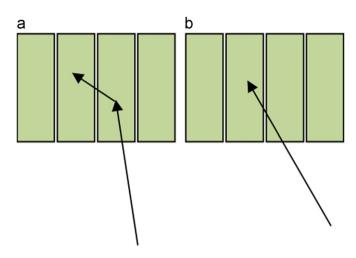
Fig. 1. An example of a photon experiencing (a) ICS and (b) penetration in a typical detector block.

entered after one or more compton interactions and hence deposits some of its energy in one or more crystals other than the initial crystal. Fig. 1 a and b depicts an example of a photon experiencing, respectively, ICS and penetration in a typical detector block. Both ICS and penetration have deteriorative impact on spatial resolution of PET scanners because they cause some photons to be detected in crystals not corresponding to the position of the annihilation from which the photon is emitted. The consequence of this photon mispositioning is that the coincidences in which at least one of the two photons mispositioned due to ICS or penetration are likely registered in incorrect line of responses (LORs). In addition, the current trend of PET detection system implementation that leans toward fabrication of smaller crystals for reaching better intrinsic spatial resolution worsens the impact of ICS and penetration due to the higher probability of the photon escape from the prime crystal before interaction or after compton interaction.

Nonetheless, following the introduction and utility of statistical image reconstruction methods in PET and the so-called system matrix, it has been shown that it is possible to compensate for ICS and penetration by accurately modeling their effects within the projection space [2–9]. In contrast to conventional post-reconstruction partial volume correction (PVC), this approach can be viewed as reconstruction-based PVC [10]. An understanding of the quantitative behavior of ICS and penetration plays an important role whether in design of a more optimized PET detection system or in more accurate modeling of ICS and penetration effects for modification of system matrix in order to enhance the quality of reconstructed images.

To the best of our knowledge, up to now the studies performed on quantification of ICS and inter-crystal penetration have primarily (and even merely) concentrated on single 511 keV photons instead of considering coincidences [11–14]. By contrast, PET detection systems are based on coincidences and therefore a single-photon-based study may not provide sufficient measurements due to the fact that singles (single photons detected in contrast to coincidences) by themselves are not of importance; the coincidences arranged in LORs are meaningful for the purpose of image reconstruction. Hence, it is more meaningful to assess the impact of ICS and penetration on mispositioning of coincidences. In this work, we evaluated the quantity of ICS and penetrated events in the form of coincidences in the PET subsystem of three members of GE whole-body PET/CT scanners: Discovery RX (DRX), Discovery ST (DST), and Discovery STE (DSTE). Foremost, as a novel study, we discriminated between

penetrated events and ICS events. Since discrimination of ICS and penetrated events is not feasible practically, Monte Carlo (MC) approaches are considered the most reliable ones for this aim. In order to do this, we employed GATE (Geant4 Application for Tomographic Emission) MC toolkit [15] and used our previously validated models of DRX, DST, and DSTE [16].

2. Material and methods

2.1. GATE Monte Carlo modeling of the PET scanners

Although the DRX, DST, and DSTE are integrated PET/CT scanners, our focus in this study was on the PET subsystem. As such, the emphasis of this section is to describe the PET scanners' features relevant to the task of implementing the MC model. GATE v4.0.0 (Geant4 Application for Tomographic Emission) MC code [15] was used for MC simulations. As mentioned earlier, we used our previously validated MC models [16] in this work.

The act of classification of the DRX, DST, and DSTE in one family is meaningful because they have many common features. Their dominant differences are in the crystal materials and crystal sizes utilized. All three scanners follow the block-detector structure in which arrays of subunits (so-called modules) are repeated. Modules, being subunits of the blocks, are composed of an array of crystal elements.

The crystal dimensions in DRX are $4.2 \times 6.3 \times 30$ mm^3, while they are repeated 9×6 times in transaxial and axial directions, respectively, to form a module. An array of 2×4 modules in, respectively, transaxial and axial directions builds a block. Replication of 35 blocks around an 88.6 cm-diameter ring composes the DRX detection system. Likewise the dimensions of the DST crystals are $6.25 \times 6.25 \times 30$ mm^3, and an array of 6×6 crystals constructs a module. In addition, each block includes 2×4 modules in transaxial and axial directions, respectively. The DST detection system is also composed of 35 replicas of the blocks in an 88.6 cm-diameter ring. Similarly, the DSTE crystal dimensions are $4.7 \times 6.3 \times 30$ mm^3, and duplication of 8×8 crystals builds a module. The blocks are as well composed of 2×3 modules in transaxial and axial directions, respectively. In the same manner as the other two scanners, the detection system of the DSTE consists of 35 replicas of the blocks in an 88.6 cm-diameter ring. Furthermore, axial and transaxial fields of view (FOV) of the three scanners are nominally 15.7 cm and 70 cm, respectively. The crystal material in DRX is Cerium-doped Lutetium Yttrium Orthosilicate (LYSO). By contrast, the crystals are made from Bismuth Germinate (BGO) in the DST and DSTE. All physical features of the PET scanners were implemented in the MC models. In the GATE MC models, the coincidence window was set to 5.85 ns, 11.7 ns, and 9.75 ns for DRX, DST, and DSTE, respectively [13,14,16,18,19]. The lower energy threshold was adjusted to 375 keV for DST and 425 keV for both DRX and DSTE. Furthermore, the upper energy threshold was set to 650 keV for all three systems. In addition, the shielding of the scanners, the inter-crystal septa, and the electronic properties of the readout system were taken into account in the modeling [16–22]. The characteristics of the detection system for DRX, DST, and DSTE are summarized in Table 1.

2.2. Proposed method for discrimination of ICS and penetration

Although the discrimination of mispositioned coincidences may be achieved in practice by point source measurements across multiple FOV positions the measurements may need to be made very precisely, and the determination and decoupling of factors causing the mispositioning can be difficult [4]. MC simulations coupled with advanced post-processing techniques provide a

convenient approach to this problem to circumvent both issues. In our simulations, we employed an ideal 511 keV point source (i.e. dimensionless and free from positron range and photons non-collinearity). As such, there were no mispositioned coincidences induced by these non-idealities. In addition, we evaluated the entirety of FOV with no extended attenuating medium so that no scattering was possible inside the FOV. Finally, before data analysis, we deleted all random coincidences from the database. Consequently the only factor resulting in coincidence mispositioning was ICS and/or penetration (ICS–P), which could also be distinguished from one another within the MC framework, as described next.

An in-house software was developed for discrimination and categorization of different types of coincidences stored in the output file of GATE after every simulation. As mentioned before, due to implementing a special condition in the MC simulation, no scatter coincidence existed in the output. In addition, random counts were not considered in the process. For distinguishing mispositioned coincidences from those that were correctly registered as true coincidences (purely true coincidences), the in-house software examined each true coincidence to identify whether the spatial volume composed of the two corresponding detector elements of the two singles (so-called tube of response (TOR)) included the known position of the point source. If the point source was inside the TOR, it meant that the coincidence was purely true; otherwise it was mispositioned because of ICS–P. Furthermore, as GATE registers the number of intra-detector Compton interactions of every single event of the coincidence pair prior to absorption or escape from the scanner (in the form of so-called *comp_det* variable), we categorized the mispositioned coincidences into three groups based on three possible conditions for *comp_det* variables of the singles in a coincidence, namely
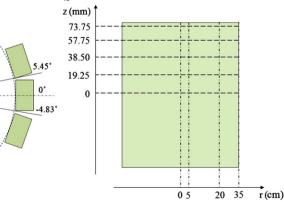
group-1, group-2, and group-3. Group-1 consisted of coincidence events with event(s) only affected by penetration (one or both). Group-2 included coincidences where one event was affected by ICS (possibly including penetration), while the other event was not affected by ICS (i.e. it experienced penetration or no mispositioning at all). Finally in group-3, both coincidence events were affected by ICS (possibly also including penetration).

While our primary goal in this work was to obtain a quantitative viewpoint from ICS–P we defined a metric, the system response function (SRF), to further illustrate the effect of ICS-P mispositioned coincidences in the projection domain. Given that ICS-P mispositioning alters the azimuthal angle of a given LOR in a relatively minor way [5] the SRF we defined showed the distribution of a point source response after axial rebinning along the radial and axial directions, assuming negligible mispositioning in the angular direction in each slice. In order to obtain the SRF for each point source location in the DRX, 3D data were rebinned using the Single Slice Rebinning (SSRB) algorithm [23] into 47 2D sinograms with 323 radial bins and 315 angular bins (the same as the 2D sinogram size in the real system) without any limitation for maximum ring difference. The SRF for each source position was arranged in a 25×23 array; horizontal direction (25 bins) quantifies the signed difference between the radii in the registered event and the known source position, with bin sizes of 2.17 mm, and the vertical direction demonstrates signed difference between the axial position of the registered event and the known source, with bin sizes of 3.27 mm.

Moreover, using a post-processing algorithm applied on 3D registered LORs, we calculated the deviation of mispositioned LORs from the known position of the source for different source radial positions. For this, the line that connects the centers of the two corresponding detector pixels in each LOR was formulated and its distance from the source position was computed in 3D space as the LOR deviation.

2.3. Monte Carlo simulations

The best way to quantitatively analyze ICS and penetration in the entire FOV, as accurately as possible, is to sample all possible positions inside the FOV via simulated point sources. Nevertheless this poses a very expensive and time-consuming task from the perspective of both the simulation and post-processing efforts and, furthermore, it will generate extensive volumes of generated data. In order to overcome this issue, we utilized geometrical symmetries of the scanners and acquire the critical direction(s) along which quantitative behavior of ICS and penetration was notable though, similar to other studies [4,5], the

Table 1
Detection system characteristics of the DRX, DST, and DSTE scanners.

	DRX	DST	DSTE
Crystal material	LYSO	BGO	BGO
Crystal pitch—axial(mm)	6.4	6.35	6.4
Crystal pitch—transaxial(mm)	4.3	6.35	4.8
Crystal depth (mm)	30	30	30
No. of crystals per module	9×6	6×6	8×8
No. of modules per detector block	2×4	2×4	2×3
No. of detector blocks	35	35	35
No. of rings	24	24	24
No. of crystals per ring	630	420	560
Ring diameter (cm)	88.6	88.6	88.6
Axial FOV (cm)	15.7	15.7	15.7
Transaxial FOV(cm)	70	70	70

Fig. 2. (a) Cross-section of the DRX gantry in which the bold line and the bold arc are the locus of points assessed in radial direction and angular direction, respectively; (b) Top view of the DRX gantry in which the locus of investigated points in axial direction are shown. The dimensions in Z-direction are exaggerated.
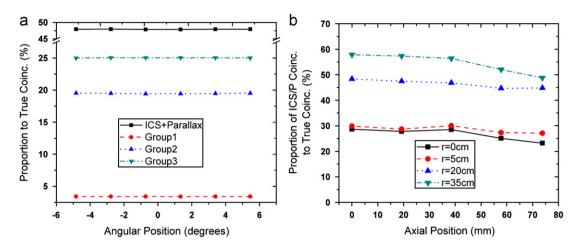
Fig. 3. Proportion of ICS–P coincidences to true coincidences in DRX (a) along the angular direction in one angular period at a radius of 20 cm and (b) along the axial direction at four different radial positions.

expectation was to observe the most significant variations along radial direction. DRX was chosen for this comprehensive analysis. As mentioned earlier, the DRX detection system consists of 35 blocks. It can be seen in Fig. 2a that the geometry of the DRX is generated by replicating a block rotated transaxially along a particular angle ($\gamma = 10.29°$). By obtaining the profiles of ICS and penetration along one angular interval (shaded region in Fig. 2a), one can deduce the behavior along the entire 360° ring. According to the cylindrical shape of the system, the two halves of the DRX along the axial direction are symmetrical. Hence having the behavior of ICS and penetration along one axial half, the behavior can be extended for the other half. The lines resulting from connecting the positions of the points at axial center sampled in angular and radial directions are illustrated in Fig. 2a. Also, the axial and radial offsets of the positions assessed in one half of the axial direction are shown in Fig. 2b. For angular analysis, six points at the axial center and radius of 20 cm were assessed (Fig. 2a, starting from $-4.83°$ to $5.45°$ by angular steps of $2.06°$. For axial analysis, five axial positions along one half of the cylinder were chosen ranging from the axial center ($z = 0$ mm) to approximately the edge of axial FOV ($z = 73.75$ mm). In each of these steps, four radial positions (0, 5, 20 cm, and 35 cm) were investigated. Finally, since there was no symmetry along radial direction, and also because it was expected that the most significant variations of either qualitative or quantitative behavior of ICS and penetration occurs in this direction we assessed numerous radial positions at the axial center.

The comprehensive evaluation of ICS and penetration in DRX (as presented in the next section) revealed that the variations of ICS and penetration quantity along axial and in particular angular directions are minor enough to be neglected for precise investigation. Therefore, due to geometrical similarities of DRX, DST, and DSTE, we focused measurements on radial direction for DST and DSTE. For this, numerous radial positions at the axial center of DST and DSTE were appraised from ICS and penetration points of view with the same conditions and considerations as applied in the case of DRX.

3. Results

In all steps of simulation, data acquisition time was chosen to be long enough in order to obtain adequate number of coincidence events to minimize statistical errors with respect to the number of coincidence events in clinical condition. Since the sensitivity varies with the source position, acquisition time changed for each position to record approximately the same

quantity of coincidence events in each scanner. In this manner, acquisition times in DRX varied between 2570 s and 32410 s. This range was 2000–3000 s in DST and 2500–2900 s for DSTE. The point source activity was 100 kBq. The processing of output data of MC simulation was performed using the aforementioned in-house software following data acquisition. Since we aimed to evaluate the proportion of coincidence events undergoing ICS–P, the quantity of ICS, and penetration was calculated in terms of the percentage of the true coincidences mispositioned due to ICS–P.

Fig. 3a shows the proportion of the ICS–P coincidences to true coincidences for a range of angles ($10.29°$) at the axial center and a radius of 20 cm in the DRX. It is readily observed that the quantitative variations of the three groups ICS-P are negligible along the angular direction. Fig. 3b illustrates the quantity of ICS–P at four different radii along the axial direction in the DRX. As seen in Fig. 3b, the variations of ICS-P along the axial direction (at radii of 5 cm and 20 cm) are less than 5% (see the Discussion section for explanation of this effect). In addition, the quantitative trends of the three groups and the total ICS–P coincidences along the radial direction are illustrated in Fig. 4a. The total fraction of ICS–P coincidences starts from about 30% at the center of the transaxial FOV and exceeds 55% at the end of the transaxial FOV.

Subsequently, we focused our efforts to assess the behavior of ICS and penetration in DST and DSTE only along the radial direction. Fig. 4b and c shows the quantity of ICS–P together with the three groups in DST and DSTE, respectively. The amount of ICS–P coincidences at the end of the transaxial FOV exceeds 45% in both DST and DSTE. In order to provide a comparison between the quantity of ICS–P coincidences in DRX, DST, and DSTE, the proportion of ICS–P coincidences to true coincidences of the three scanners are sketched together in Fig. 4d.

Fig. 5 shows the SRFs of the mispositioned events extracted for a point source at axial center and the radii of 0 cm, 20 cm, and 35 cm in DRX based on the definition introduced earlier Section 2.2. As seen in Fig. 5, with increasing radii, the undesirable spatial distribution of events gets worse.

Finally, as described in Section 2.2, the various proportions of deviations of mispositioned LORs were calculated and plotted for DRX as shown in Fig. 6, and repeated for different radial positions of the source ranging from 0 cm to 35 cm. The deviation values were binned into 10 bins with sizes of 5 mm each; i.e. LOR deviations between 0 mm and 5 mm were counted together in bin #1, ones between 5 mm and 10 mm counted in bin #2, and so on. Since the number of LORs with deviations greater than 50 mm was negligible, larger deviations than 50 mm are not shown in the plot. For each source position, the deviated counts in each bin
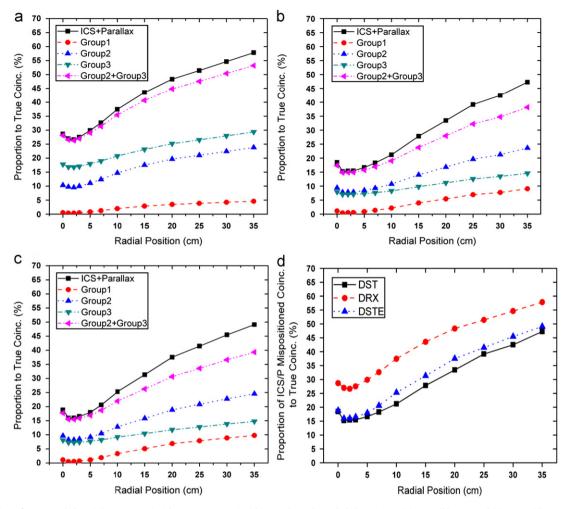
Fig. 4. Proportion of ICS–P and the triple groups coincidences to true coincidences along the radial direction in (a) DRX, (b) DST, and (c) DSTE. (d) Comparison of ICS–P coincidences in the DRX, DST, and DSTE.

were normalized by the sum of mispositioned events in that position to obtain the proportion of events in each deviation bin with respect to total mispositioned events. In addition, spline fitting was applied for all curves to provide better visualization.

4. Discussion

Fig. 3a reveals that the quantitative behavior of the ICS and penetration in DRX is effectively constant with variations in the angular position. Since the full ring is composed of 35 replicated angular regions and the behavior of ICS and penetration in each region is the same, it follows by symmetry that the quantity of ICS–P coincidences along the entire 360° ring is constant for each radial position. This statement also follows for other scanners that have a similar geometry to the DRX.

In addition, Fig. 3b shows that the proportion of ICS-P coincidences to true coincidences in the DRX slightly decreases as the source becomes more distant from the axial center ($z=0$ mm) and closer to the edge of the axial FOV. The reason is that with respect to the characteristic of coincidence detection, as the source travels from the axial center towards the axial FOV edge, the range of probable angles[1] for annihilation photons to be detected

[1] The angle between the photon trajectory and the normal vector of the crystal surface.

in coincidence becomes narrower. The maximum probable angle of detection for coincidence photons emitted from the axial center can be approximately calculated as

$$\tan^{-1}\left(\frac{\text{axial FOV}/2}{radius}\right) \tag{1}$$

On the contrary, this angular range drops to nearly zero for coincidence photons emitted at the edge of the axial extent. Fig. 7 depicts an exaggerated schematic indicating the range of allowed photon angles at two axial positions: the axial center ($z=0$ mm) and $z=73.75$ mm. The maximum allowed angle at the axial center and at $z=73.75$ mm are, respectively, about 9.8° and 0.4°. As a result, the probability of photons undergoing penetration (and also ICS) becomes smaller as the source gets closer to the edge of the axial extent. Lashkari et al. [13] using MC simulation have shown that the increment of the incident 511 keV photon angle from 0° to 10° results in about 3% increase in the percentage of ICS for a single in a $4 \times 4 \times 20$ mm^3-crystal array. Likewise, supposing that the probability of a perpendicular photon for penetration is zero, the increment of the photon angle from 0° to 10° causes about 35% increase in the percentage of penetrated single photons [13]. As evident from Fig. 3b, since the quantity of ICS-P coincidences is larger at greater radii its variation along the axial position is also more extensive.

Figs. 4a to c proves that while conventional theoretical explanations may expect that the amount of ICS–P is minimal at the center of the transaxial FOV ($r=0$), the minimum may occur at
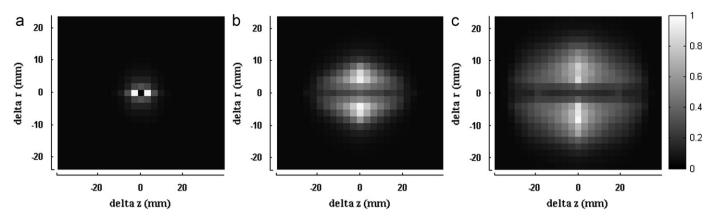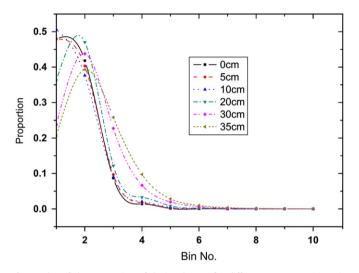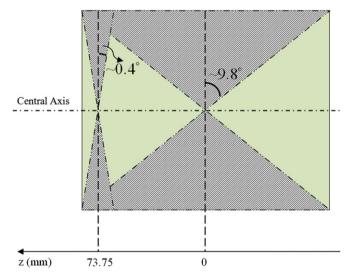
Fig. 5. SRFs of the "mispositioned" events at radii of 0 cm (a), 20 cm (b), and 35 cm (c) at axial center in the DRX. The SRFs were normalized by their maximum value. While vertical axis demonstrates the deviation of the LOR radius from the correct known value, horizontal axis shows the axial deviation.

Fig. 6. Plot of the proportion of deviated LORs for different source positions in DRX. Horizontal axis shows the deviation bins, each with a size of 5 mm. Spline fitting was applied for better visualization.

Fig. 7. An exaggerated schematic indicating the range of the allowed photon angle for two axial positions.

other radii for a scanner composed of *blocks* of detectors. Furthermore the non-zero value for group-1 at the transaxial center, indicating presence of penetration-induced mispositioned

coincidences, is firstly due to the above description for non-minimal values at the center, and secondly because of 3-dimensinal data acquisition in which axially oblique lines of response lead to non-zero probability for penetration.

Fig. 4d provides a comparison of ICS–P distributions in DRX, DST, and DSTE. As can be seen, the plot for the DRX depicts a notable difference with those of the DST and DSTE. The reason is that the crystal size in the DRX is smaller to some extent in comparison with the other two scanners. In addition, the DRX scintillation crystal is made of LYSO that has a smaller attenuation length and also photofraction compared to the BGO crystal in DST and DSTE [24]. These factors cause the incident photon to have a greater chance of escaping the DRX crystals on which they are incident in contrast with the DST and DSTE crystals, whether with or without experiencing any Compton interactions; this results in a greater fraction of ICS–P coincidences in the DRX. The quantities of ICS–P coincidences in the DST and DSTE are almost the same. However; the smaller value of ICS–P events in the DST is mainly due to having larger crystals.

Although reconstruction of images without and with coincidence events affected by ICS–P could provide additional quantitative measures for assessing the impact of ICS–P mispositioned events within the image domain, the statistics of the events obtained by our Monte Carlo simulation are not yet sufficient for being utilized for image reconstruction tasks. We are presently working on enhanced MC methods, given our computational facilities, to generate sufficient data for extensive image-based analysis. At the same time, additional demonstrations using the SRF measure can still help to evaluate a number of ICS–P effects within the projection domain.

Fig. 5 provides an illustration of the effect of the ICS-P mispositioned coincidences. Fig. 5a to b demonstrates that the SRFs of the mispositioned events have a hot line along radial direction, showing that the dominant mispositioning occurs along the radial direction for the axial plane of the point source. Although part of the distribution along the axial direction is due to SSRB errors, the role of ICS-P mispositioning in the axial distribution of the SRFs cannot be neglected: the bins corresponding to small radii in the SRFs have low values, depicting that that those events mostly belong to purely true category. As seen the SRF at the end of the transaxial FOV (35 cm) widens by about 30 mm along the axial direction and about 20 mm along radial direction, which expected due to the size of the crystals and also rebinning error.

Fig. 6 demonstrates that as the source radial offset increases, so does the deviation of mispositioned LORs from the expected location. Although the deviation of the LORs at 0 cm, 5cm, and 10 cm is almost the same, it gets larger by moving the source from 10–35 cm. Widening the curves in Fig. 6, from 10 cm to

35 cm, tells the same story. The so-called parallax effect, namely the degradation in spatial resolution of PET images along the radial direction, can be observed from the obtained results: as the radial offset of the source increases not only does the amount of ICS–P mispositioned events raises, but also their deviations from the true position become larger. This ultimately translates to a degradation in spatial resolution with increasing radial offsets.

5. Conclusions

An algorithm was developed in this work to process the Monte Carlo data for distinguishing between purely true coincidences and those mispositioned due to ICS and/or penetration. The results, as expected, showed that the largest variations of ICS–P quantity happen along the radial direction. In addition, our results obtained from comprehensive assessment of the ICS–P quantity in the DRX revealed that the fluctuation of ICS–P amount along axial and especially angular directions is so small that it can be neglected. It is more meaningful to concentrate simulation efforts to study radial variation of the ICS–P contributions in PET geometries similar to the Discovery PET/CT family.

Following the current results our future work consists of incorporating the simulated effects within the system matrix of each scanner to study and compare resolution modeling technique aiming to compensate for the deteriorative effects of ICS and penetration on image quality, as applied to the three above mentioned scanners.

Acknowledgments

References

[1] A. Rahmim, H. Zaidi, Nucl. Med. Commun. 29 (2008) 193.
[2] J. Qi, R.M. Leahy, S.R. Cherry, A. Chatziioannou, T.H. Farquhar, Phys. Med. Biol. 43 (1998) 1001.
[3] V.Y. Panin, F. Kehren, H. Rothfuss, D. Hu, C. Michel, M.E. Casey, IEEE Trans. Nucl. Sci. 53 (2006) 152.
[4] V.Y. Panin, F. Kehren, C. Michel, IEEE Trans. Med. Imag 25 (2006) 907.
[5] A.M. Alessio, P.E. Kinahan, T.K. Lewellen, IEEE Trans. Med. Imaging 25 (2006) 828.
[6] A. Rahmim, J. Tang, M.A. Lodge, S. Lashkari, M.R. Ay, R. Lautamaki, B.M. Tsui, F.M. Bengel, Phys. Med. Biol. 53 (2008) 5947.
[7] S. Moehrs, M. Defrise, N. Belcari, A.D. Guerra, A. Bartoli, S. Fabbri, G. Zanetti, Phys. Med. Biol. 53 (2008) 6925.
[8] J.E. Ortuno, G. Kontaxakis, J.L. Rubio, P. Guerra, A. Santos, Phys. Med. Biol. 55 (2010) 1833.
[9] S. Stute, D. Benoit, A. Martineau, N.S. Rehfeld, I. Buvat, Phys Med Biol 56 (2011) 793.
[10] O. Rousset, A. Rahmim, A. Alavi, H. Zaidi, PET Clin. 2 (2007) 235.
[11] Y. Shao, S.R. Cherry, S. Siegel, R.W. Silverman, IEEE Trans. Nucl. Sci. 43 (1996) 1938.
[12] E. Yoshida, K. Kitamura, Y. Kimura, F. Nishikido, K. Shibuya, T. Yamaga, H. Murayama, Nucl. Instr. and Meth. A 571 (2007) 243.
[13] S. Lashkari, S. Sarkar, M.R. Ay, A. Rahmim, IFMBE Proc. 21 (2008) 633.
[14] S. Rechka, R. Fontaine, R. Lecomte, M. Rafecas: Labpet inter-crystal scatter study using gate, in: IEEE Nuclear Science Symposium Conference Record (NSS/MIC),. Orlando, FL, 2009, pp. 3988–3994.
[15] S. Jan, G. Santin, D. Strul, S. Staelens, K. Assie, D. Autret, S. Avner, R. Barbier, M. Bardies, P.M. Bloomfield, D. Brasse, V. Breton, P. Bruyndonckx, I. Buvat, A.F. Chatziioannou, Y. Choi, Y.H. Chung, C. Comtat, D. Donnarieix, L. Ferrer, S.J. Glick, C.J. Groiselle, D. Guez, P.F. Honore, S. Kerhoas-Cavata, A.S. Kirov, V. Kohli, M. Koole, M. Krieguer, D.J. van der Laan, F. Lamare, G. Largeron, C. Lartizien, D. Lazaro, M.C. Maas, L. Maigne, F. Mayet, F. Melot, C. Merheb, E. Pennacchio, J. Perez, U. Pietrzyk, F.R. Rannou, M. Rey, D.R. Schaart, C.R. Schmidtlein, L. Simon, T.Y. Song, J.M. Vieira, D. Visvikis, R. Van de Walle, E. Wieers, Phys. Med. Biol. 49 (2004) 4543.
[16] P. Geramifar, M.R. Ay, M. Shamsaie, G. Loudos, A. Rahmim: Monte carlo based performance assessment of four commercial Ge Discovery Pet/Ct scanners using gate, in: IEEE Nuclear Science Symposium Conference Record. Dresden, Germany, 2008, pp. 3995–3999.
[17] GE-Healthcare: Discovery rx 16 product data, 2006.
[18] B.J. Kemp, C. Kim, J.J. Williams, A. Ganin, V.J. Lowe, J. Nucl. Med. 47 (2006) 1960.
[19] H. Baghaei, O. Mawlawi, Y. Wang, H. Li, R. Ramirez, S. Kim, Y. Zhang, T. Pan, J. Liu, S. Liu, W.-H. Wong A comparison of five whole-body Pet scanners by scanning hoffman brain phantom, in: IEEE Nuclear Science Symposium Conference Record, 2006, 4, pp. 1973–1976.
[20] M. Teras, T. Tolvanen, J.J. Johansson, J.J. Williams, J. Knuuti, Eur. J. Nucl. Med. Mol. Imaging 34 (2007) 1683.
[21] GE-Healthcare Discovery ste 8 product data, 2006.
[22] P. Geramifar, M.R. AY, M. Shamsaii Zafarghandi, G. Loudos, A. Rahmim: Monte carlo simulation of the Ge LYSO-based discovery Rx Pet/Ct scanner using gate: a validation study, in proceedings the Annual Congress of the European Association of Nuclear Medicine (ENAM), Abstract 296, 2008.
[23] M.E. Daube-Witherspoon, G. Muehllehner, J. Nucl. Med. 28 (1987) 1717.
[24] H. Zaidi, B.H. Hasegawa, Overview of nuclear medical imaging: physics and instrumentation, in: H. Zaidi (Ed.), Quantitative Analysis in Nuclear Medicine Imaging, Springer, Singapore, 2006.